Centrifugal atomization of stainless-steel rotating rods melted by a high-power LASER beam

B. Ravry, A. Mathieu, J. Allenou, B. Sinardet, S. Pernot, F. Bernard, B. Stepnik, F. Demoisson

Version of Record: https://www.sciencedirect.com/science/article/pii/S0921883122002096
Manuscript_62918026d498f67e2b200ee9f7538869

Centrifugal atomization of stainless-steel rotating rods melted by a high-power LASER beam

Authors:

B. Ravry[1*], A. Mathieu[1], J. Allenou[2], B. Sinardet[1], S. Pernot[1], F. Bernard[1], B. Stepnik[2], F. Demoisson[1]

*Corresponding author: bastien_ravry@etu.u-bourgogne.fr

[1]Laboratoire ICB – UMR 6303 CNRS / UBFC, 9 Avenue Alain Savary, 21000 Dijon, France

[2]Framatome CERCA™, ZI les Bérauds BP 1114, 26104 Romans-sur-Isère, France

1 Introduction:

Powder metallurgy processes like spark plasma sintering (SPS) or additive manufacturing (AM) have great potential for industrial application, as they are capable of producing complex and near net shape parts with enhanced mechanical properties compared to traditional processes [1]. In these applications, the quality of the parts directly depends on the quality of the powder. As particle size, sphericity or chemical composition (including purity) will directly affect the microstructure of the final product [2–4], it is essential to produce high-quality powders to guarantee the best properties for the final part. Gas and water atomizers were widely developed due to their great productivity and efficiency in producing micron-size particles [5]. However, particles can be hollow, non-homogeneous in chemical composition and possess a large particle size distribution due to non-solidified particle collisions [5–7]. The rotating electrode process (REP) has the advantage of preventing these problems via a high cooling rate, reduced segregation and a narrow particle size distribution. The powders produced are spherical with high purity [8,9] and particles are ejected near the melting temperature. Solidification occurs rapidly, i.e. 10^2 K.s $^{-1}$ to 10^4 K.s^{-1}, thus high-reactivity powders, such as titanium or molybdenum, can be produced with this process since external contamination is prevented from the ball milling process and gas or water in the atomization tower [10,11].

This study aims to prove the feasibility of using a LASER beam as a heating source instead of an electrical arc in REP. REP is affected by electrical arc instability due to a vortex induced by a high-speed rotating electrode in a gas environment. Electrode-to-piece distance between the rod surface and the tungsten electrode is complex to control and induces an arc voltage variation modifying the deposited

energy. Tungsten contamination is also possible which disqualifies the REP process from high-purity powder production [1]. The LASER solution also makes it possible to avoid the passage of the electrical current through the spindle and thus enabling higher ejection speeds to reduce particle size. Previous studies on REP using a LASER source were conducted in a specific configuration [11,12] and we propose to go further by implementing a high-speed imaging technique to study the process and to identify the atomization regime as well as monitor irregular particle production that reduces overall production yield of a spherical powder.

This study also focuses on particle characteristics, depending on the process parameters, such as the incident LASER beam power density, particle ejection speed and atomization surrounding atmosphere. Experimental results on the particle size and the atomization regime have been compared with prediction models from the literature.

2 Materials and methods:

The prototype outline schematic is presented in Figure 1. A stainless-steel collection chamber is set over the spindle and collects the powder under a controlled argon atmosphere. A high-speed camera was used to observe the fragmentation regimes and the particle production at a frame rate of up to 30,000 frames per second. A bichromatic pyrometer has been used to measure the temperature at the top surface of the rotating electrode during operation.

The chamber is covered with a polycarbonate plate designed to ensure the passage of the LASER beam and argon injection as well as enable camera observation. The oxygen content has been measured using a Systech EC92DIS oxygen analyzer. The LASER optic creates a spot on the rotating rods covering the entire heated surface. The high-speed camera observes the atomization process and fragmentation regimes with a frame rate of up to 30,000 fps with a 768 x 480 pixels resolution. The spindle rotation, LASER shot, high-speed camera and illumination triggers are synchronized using a 6-axes KUKA® robot system that maintains the LASER optical head. A band-pass filter was used to

observe the process and avoid camera sensor dazzling during recording and to provide a clear view of the atomization process.

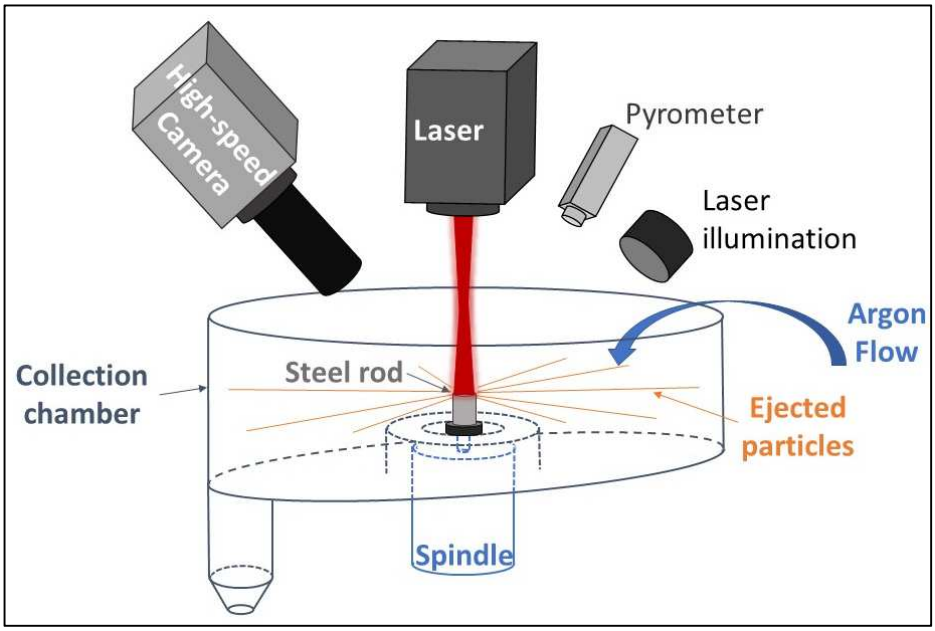

Figure 1: Schematic illustration of the REP installation using a defocused LASER beam as a heating source.

Two series of experiments have been carried out on 316L grade stainless steel rods under two different chamber atmospheres: one containing 10,000 ppm of oxygen (Atmosphere A) and the other 250 ppm of oxygen (Atmosphere B).

The rods were operated to achieve two different particle ejection speeds of 32.5 $m.s^{-1}$ and 48.7 $m.s^{-1}$. Two different incident LASER beam power densities have been used to heat the surface: 8.9 $W.cm^{-2}$ and 13.4 $W.cm^{-2}$.

Particle size distribution was measured using a dry powder LASER diffraction analyzer, Malvern Mastersizer and Sirocco 2000 with a measuring range of 0.02-2000 µm. Particles were observed using scanning electron microscopy (SEM) to evaluate the surface appearance and an optical microscope was used to measure sphericity with the Zeiss AxioVision Software which compared particle shape with a perfect circle. A 125 µm sieve was used to remove non-spherical particles from the powder. The mass proportion of each population has been measured.

3 Theory:

An advantage of REP is the limited number of parameters to set in order to optimize the properties of the produced powders. Particle sizes and shapes are mainly dependent on the rotational speed and material properties [1,13,14]. The median particle size of powders obtained by centrifugal atomization can be determined by considering the balance between capillarity and centrifugal forces. Elsewhere [1,14–16] a relationship has been proposed linking the average particle size to the material properties and the atomization process parameters as shown in Equation (1). Equation (1) is also dependent on the atmosphere as surface tension relies on the interaction between the liquid and the gas which can also be affected by oxidation [17]:

$$d_{50} = \frac{k}{\omega}\sqrt{\frac{\sigma}{\rho D}} \quad (1)$$

where d_{50} is the average particle size (m), k is a constant depending on the material and atomizer configuration, ω is the rotational speed ($rad.s^{-1}$), D is the electrode diameter (m), ρ is the density of the liquid ($kg.m^{-3}$) and σ is the surface tension of the liquid ($N.m^{-1}$).

D_{50} means that 50% of the number of analyzed particles have a size under this value.

Another important data in rotary atomizers is the atomization regime occurring during the process. Three regimes are mainly identified for REP [18,19]: (i) direct droplet formation (DDF) where the droplets are directly ejected from the circular edge of the rod, (ii) ligament disintegration (LD) where ligaments form around the rod edge and particles are produced at their extremity and (iii) film disintegration (FD) where the ligaments grow until they merge and create a film. The DDF regime is known to produce spherical particles with satellites that are created with residual liquid carried away by the main particles. The LD regime avoids satellites as the ligament is fragmented regularly by shearing in the surrounding atmosphere. Finally, the FD regime produces irregular particles due to the instability of the liquid [20,21].

These regimes were studied by Hinze and Milborn on a rotary cup atomizer system [18,19,21]. They proposed an empirical model, Equation (2), to predict the regime involved in rotary cup atomization depending on the process and material parameters:

$$X = \frac{Q*\omega^{0.6}}{D^{0.68}} / \frac{\sigma^{0.88}}{\eta^{0.17}*\rho^{0.71}} \quad (2)$$

where ω is the rotational speed (rad.s^{-1}), D is the electrode diameter (m), ρ is the density of the liquid (kg.m^{-3}), σ is the surface tension of the liquid (N.m^{-1}), Q is the volume flow rate (m^3.s^{-1}) and η is the dynamic viscosity (Pa.s).

The limits between the regimes are defined as DDF: X < 0.07, LD: 0.07 < X < 1.33 and FD: X > 1.33.

Equations (1) and (2) were used to estimate the particle sizes and the atomization regimes that should be achieved. The 316L grade stainless steel composition is shown in Table 1. The material property data used in these equations are listed in Table 2.

Elements	C	Cr	Ni	Mo	Mn	P	S	Si
Weight %	<0.03	16-18	10-14	2-3	2	<0.045	<0.03	<0.75

Table 1: Elemental composition of 316L grade stainless steel in weight %[22].

σ at the melting point (N.m^{-1})	**ρ (kg.m^{-3})**	**η at the melting point (Pa.s)**
1.5 [17]	8.000 [22]	0.005 [23]

Table 2: Material parameters for AISI 316L stainless steel.

Volume flow rate has been calculated using Equation (3):

$$Q = \frac{m_i - m_f}{t} * \rho \quad (3)$$

where Q is the volume flow rate (m^3.s^{-1}), m_i is the initial mass of the rod (kg), m_f is the final mass of the rod (kg), t is the atomization time (s) and ρ is the density of the material (kg.m^{-3}).

High-speed recordings have been used to determine the start of the consumption of the rod using a PCC Viewer Software which provides a best estimate for atomization time to use in Equation (3).

Q values have been integrated into Equation (2) to predict the atomization regimes and compared to the recorded images. Particle ejection speed and origin of irregular particles have been investigated with the use of the recordings.

4 Results

4.1 Microscope observations

For all atmospheres and parameters, the particles were observed using optical microscopy before sieving (Figure 2). Three kinds of particles were observed: spherical, satellites and irregular particles as already reported in other REP systems [10,20,21].

No particles were found to be merged or agglomerated on larger particle or flattened due to the impact on the collection chamber walls (Figure 2 and Figure 3). The irregular particles are mostly larger than 125 µm. All of these particles are removed after sieving at 125 µm leaving behind spherical particles (Figure 2). In Figure 2(a), particles present a coloration due to oxidation while in Figure 2(b) no coloration was observed. Oxygen content affects particle surface conditions due to oxidation. Moreover, oxidation is a key factor influencing the overall atomization rate. Rod oxidized surface/ LASER Beam Irradiation coupling is more effective and induces faster rod consumption during operation. In Atmosphere B, atomization times have to be twice as long as that in Atmosphere A to produce the same amount of powder for analysis.

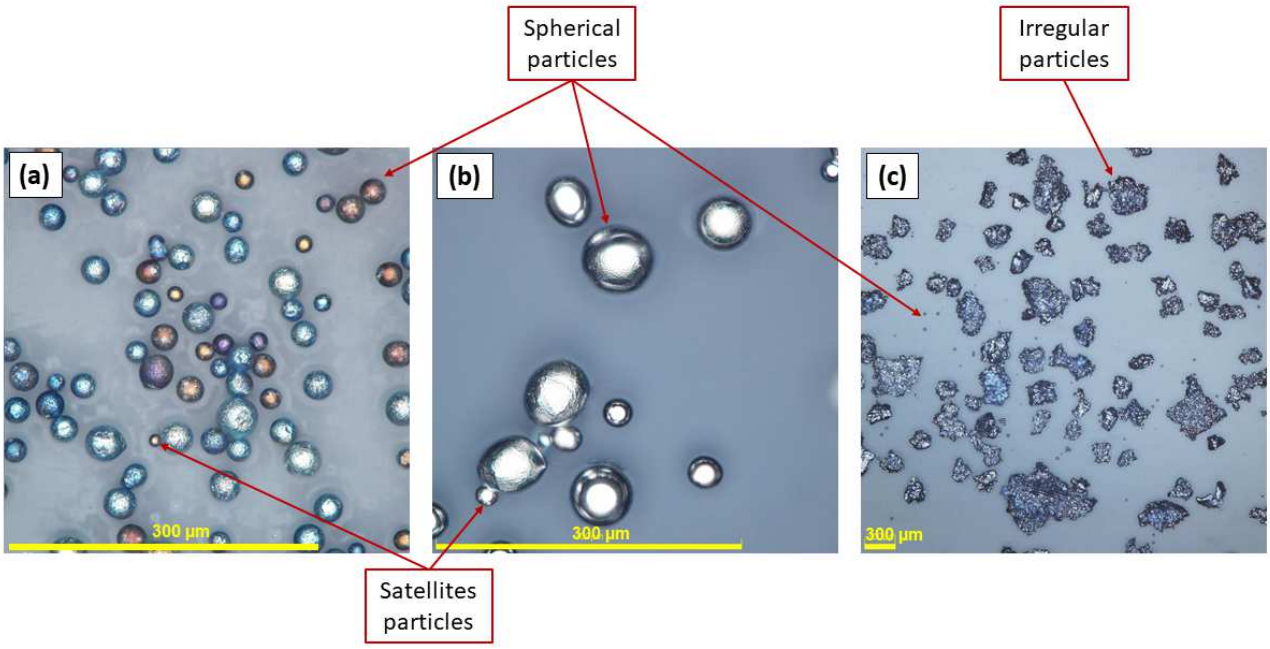

Figure 2: Microscope images of particles produced at a 13.4 W.cm^{-2} incident LASER beam power density and a 48.7 m.s^{-1} ejection speed after 125 µm sieving. (a) depicts particles exposed to Atmosphere A, (b) depicts particles exposed to Atmosphere B and (c) is an example of irregular particles (>125 µm) exposed to Atmosphere B.

The sphericity of particles has been measured using image analysis. The particles are highly spherical exhibiting 86% to 90% sphericity without any dependence on the atomization parameters (incident LASER beam power density and particle ejection speed) or atmosphere conditions (Figure 3).

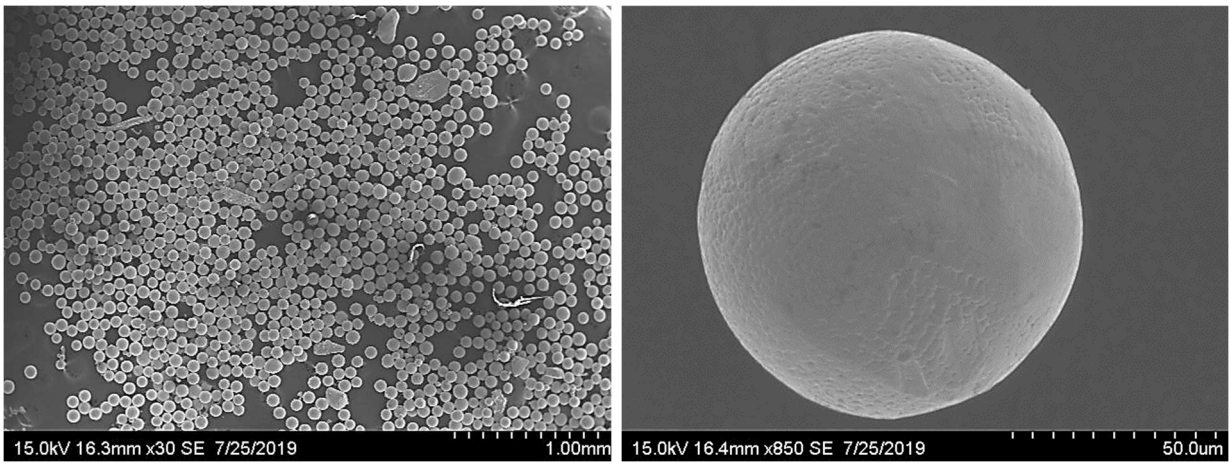

Figure 3: SEM images of particles produced at a 8.9W.cm^{-2} incident LASER beam power density and a 48.7 m.s^{-1} ejection speed in Atmosphere B.

The particle size distribution and d_{50} values have been measured for each batch by LASER diffraction measurements on the sieved dry powder.

All particle size distributions are unimodal with a narrow range as shown in Figure 4 and Figure 5.

An increase in the ejection speed reduces the mean particle size independently of the oxygen content in the atmosphere as predicted in Equation (1) and demonstrated in studies on standard REP systems [8,13,24,25]. Results show that the variation of the incident LASER beam power densities does not affect the particle size distribution no matter the atmosphere.

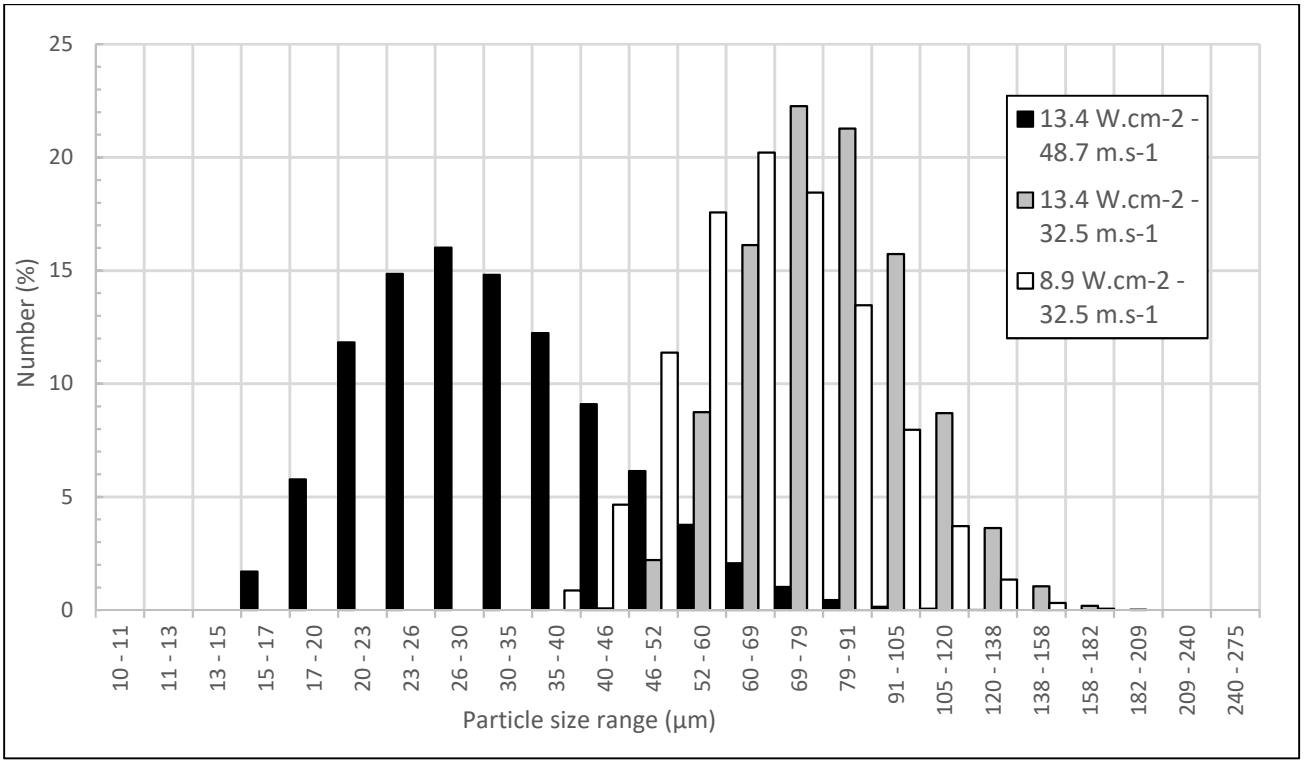

Figure 4: Particle size distribution of 316L powders prepared by REP using a LASER source at different incident LASER beam power densities and ejection speeds in Atmosphere A.

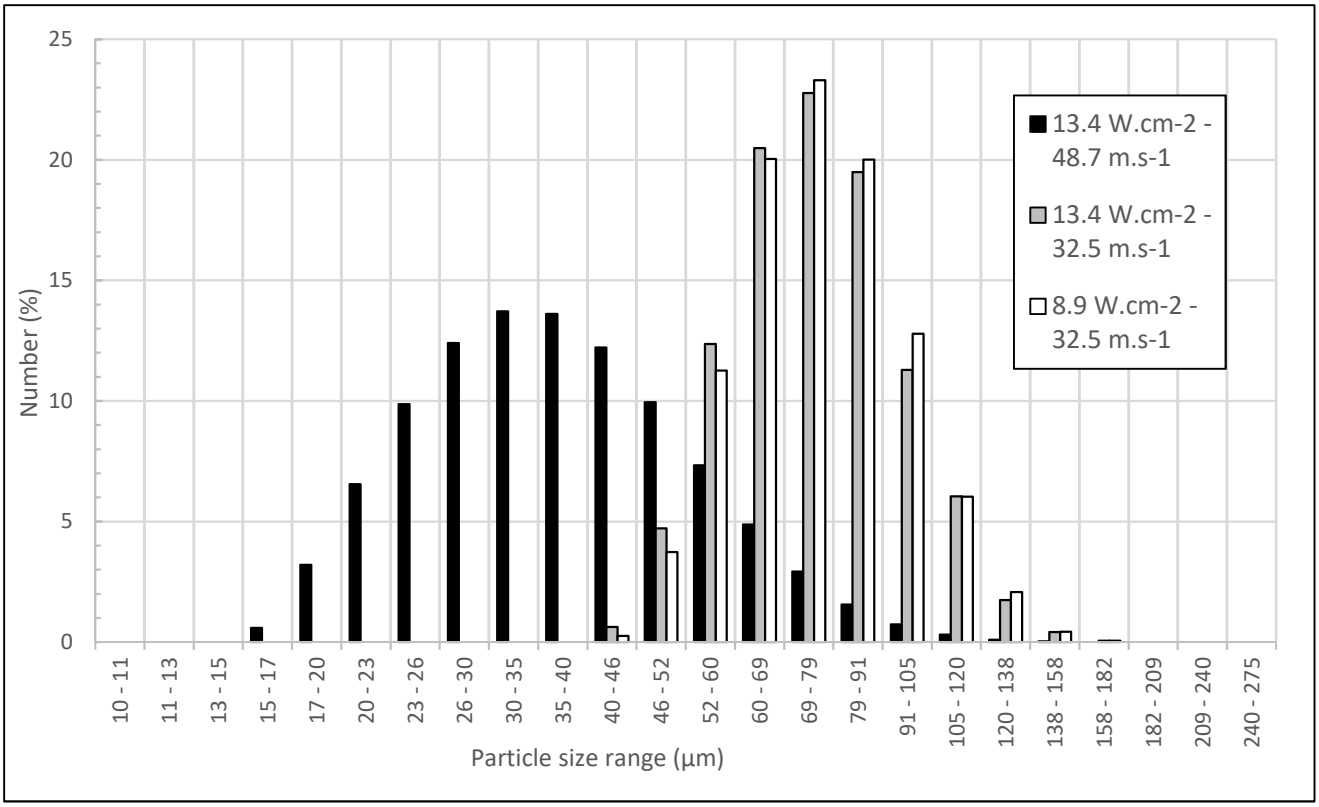

Figure 5: Particle size distribution of 316L powders prepared by REP using a LASER source at different incident LASER beam power densities and ejection speeds in Atmosphere B.

Experimental d_{50} values measured for each powder produced at different incident LASER beam power densities, ejection speeds and atmospheres are presented in Table 3. In each measurement, two batches of 2 g have been used. As seen in Figure 4 and Figure 5, incident LASER beam power density does not affect particle size hence only ejection speed should be considered for this point.

Ejection speed ($m.s^{-1}$)	LASER Power densities ($W.cm^{-2}$)	Measured d_{50} (µm)	
		Atmosphere A	Atmosphere B
32.5	8.9	64.7	75.4
			75.7
			74.9
			75.7
	13.4	79.8	75.7
			74.6
48.7	13.4	30.8	41.4
			36.4

Table 3: Comparison of d_{50} values measured by dry powder LASER diffraction on 316L grade stainless steel powders produced at different incident LASER beam power densities and ejection speeds in Atmospheres A and B.

After sieving at 125 µm, each batch has been weighed to determine the mass fraction of each population. It was found that in Atmosphere A, 85 to 96 wt.% of the powder was less than 125 µm in size, whereas only 45 to 65 wt% of the powder in Atmosphere B was smaller than this size. Moreover,

it has been noticed that particles smaller than 125 µm are totally spherical whereas particles bigger than 125 µm are mostly irregular in shape. In the last case, it has been noticed that using a higher incident LASER beam power density reduces the proportion of irregular particles.

Due to defocusing of the LASER beam relative to the rod top surface, LASER spot energy distribution is not uniform and tends to display a Gaussian distribution. In this configuration, a high proportion of irregular particles has been observed in Atmosphere B. These irregular particles are not observed for atomization in Atmosphere A since oxidation may promote beam absorption and thus LASER energy absorption too [26].

4.2 In-situ and high-speed image analysis

From high-speed imaging, irregular particles are ejected from the edge of the rod during the entire process (Figure 6 and Figure 7). This is particularly visible during the first step when melting of the complete top surface is still not achieved.

Melting of the rod surface starts at its center as this area receives more energy than the edge (Gaussian distribution) and is less affected by convection cooling due to high-speed rotation. The liquid flows over the surface that is not already melted and cools forming a solid layer. This layer tears into irregular particles under the centrifugal stresses. This phenomenon continues as the rod top surface never melts homogeneously under the LASER beam irradiation. After atomization in Atmosphere B, a crater is visible on the residual rod. This result is typical for standard REP atomization (Figure 7). However, this crater exhibits less depth with no solidified layer at the edge for atomization in Atmosphere A.

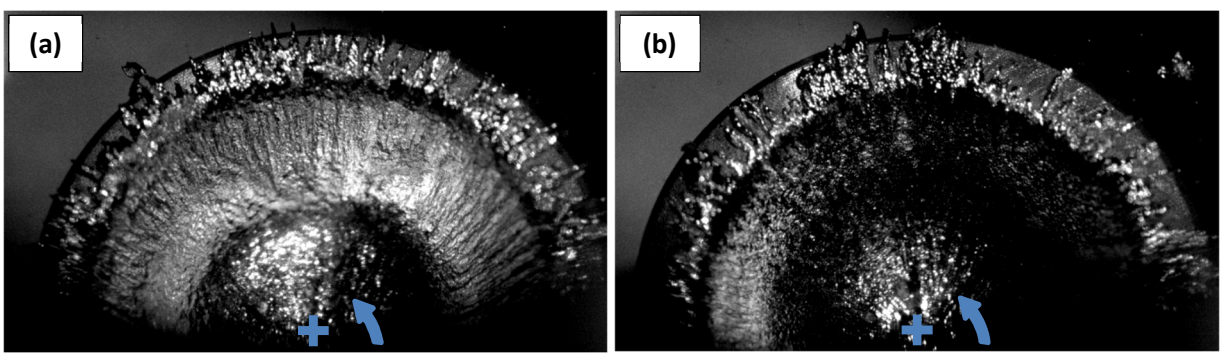

Figure 6: Images of the solid layer formation due to atomization in Atmosphere B. In (a), the conditions were an incident LASER beam power density of 8.9 W.cm^{-2} and ejection speed of 32.5 m.s^{-1} for 22.95 s and in (b) the incident LASER beam power density was 13.4 W.cm^{2} with an ejection speed of 48.7 m.s^{-1} for 13.42 s.

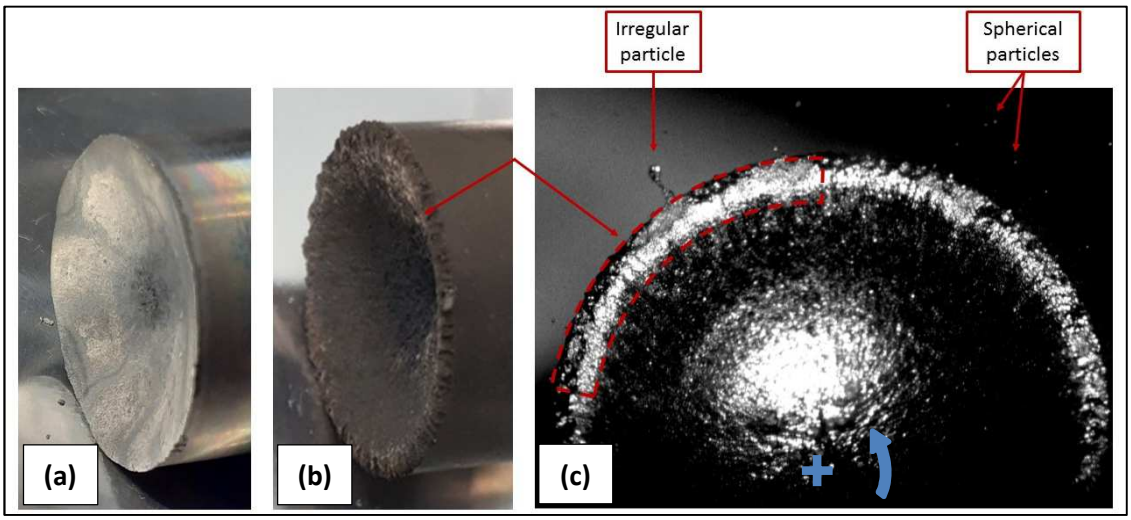

Figure 7: Images of rods after atomization using an incident LASER beam power density of 8.9 W.cm^{-2} and an ejection speed of 32.5 m.s^{-1}. (a) was performed in Atmosphere A and (b) Atmosphere B. (c) depicts irregular particles ejected from an atomized rod in Atmosphere B using an incident LASER beam power density of 8.9 W.cm^{-2} and an ejection speed of 32.5 m.s^{-1}.

In Figure 7, image (c) shows the ejection of irregular particles in Atmosphere B. The shape of this irregular particle is similar to those found in the final powder or on the residual solidified liquid at the surface of the melted rod (Figure 2). This suggests that irregular particles are already or partially solidified when ejected. A partially solidified layer can be seen at the edge of the rods where metal sheets are ejected due to centrifugal stresses and liquid flow.

Fast in-situ imaging gives indications of the atomization regime occurring during the process. For each experiment and atomization parameter, high-speed imaging shows a DDF regime in Atmosphere B and a hybrid DDF/LD regime in Atmosphere A but with only few ligaments appearing (Figure 8).

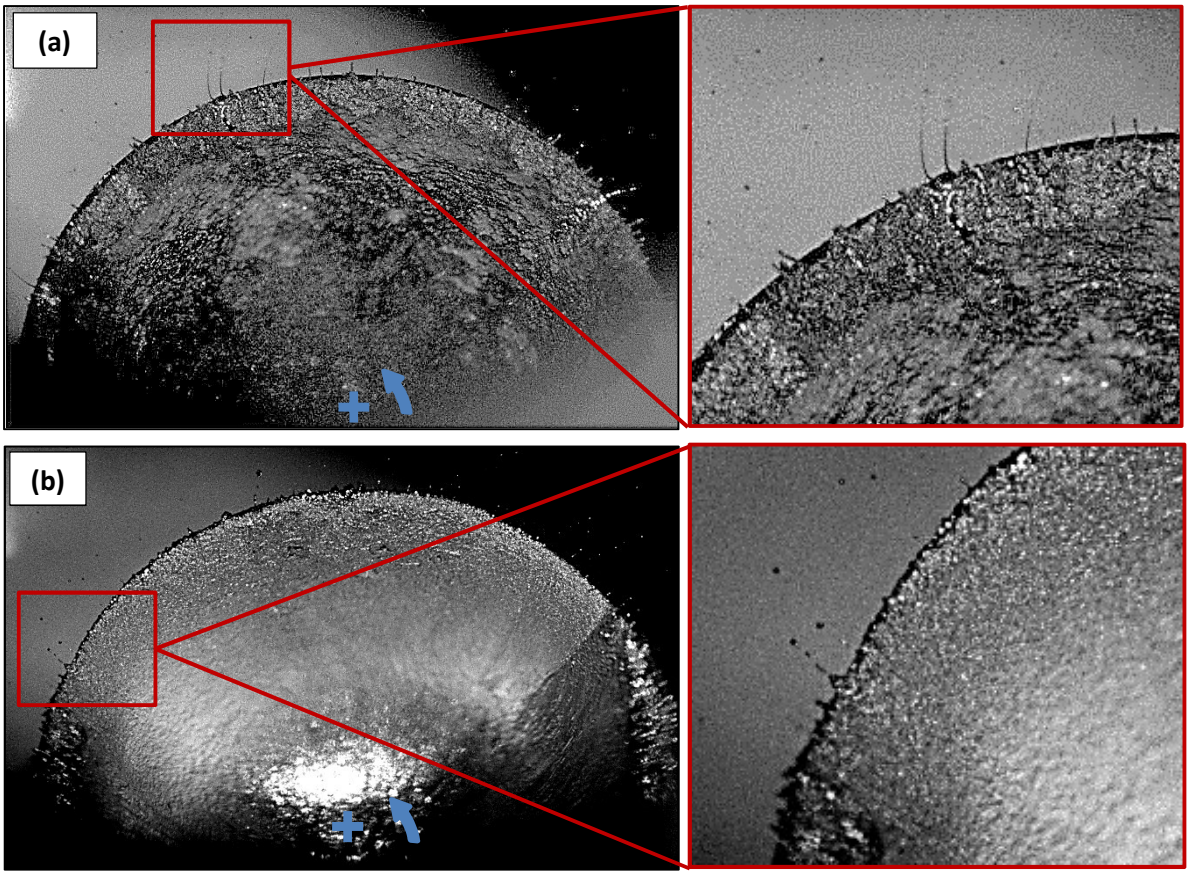

Figure 8: High-speed recorded images of the atomized rods. (a) displays the hybrid DDF/LD regime in Atmosphere A with an incident LASER beam power density of 8.9 W.cm^{-2} and an ejection speed of 32.5 m.s^{-1} after 10 s. (b) shows the DDF regime in Atmosphere B with an incident LASER beam power density of 13.4 W.cm^{-2} and an ejection speed of 48.7 m.s^{-1} after 14.56 s.

X values from Equation (2) were calculated for all atomization parameters and atmospheres which are summarized in Table 4. The volume flow rates were calculated using in-situ fast imaging information about the time where the rod consumption starts.

	LASER power density (W.cm^{-2})	Ejection speed (m.s^{-1})	X values
Atmosphere A	8.9	32.5	0.033
	13.4	32.5	0.060
	13.4	48.7	0.098
Atmosphere B	8.9	32.5	0.038
	13.4	32.5	0.059
	13.4	48.7	0.088

Table 4: X values calculated for various atomization parameters in Atmospheres A and B.

In both atmospheres, the first 2 values are coherent with the observations of a DDF regime with X <0.07 although there are some ligaments in atmosphere A, while the last value was slightly above and predicts an LD regime.

4.3 Infrared images and rod top surface temperature measurement

The high-speed camera has been used to capture infrared images of the atomization process. These images are a point of interest since they are capable of tracking the temperature evolution of the material during this process. The higher the temperature, the whiter the material appears (Figure 9).

In the beginning, liquid metal ligaments are created at the surface of the rod that is still solid. These ligaments partially cool on the solid surface and some parts are ejected creating irregular particles. Whereas fine spherical particles are ejected at the extremity of this ligament that is at a higher temperature (whiter zones shown in Figure 9 (a)). The surface continues to melt and these ligaments turn into a film until they reach the edge. The entire rod surface starts to melt and the temperature of the film becomes homogeneous.

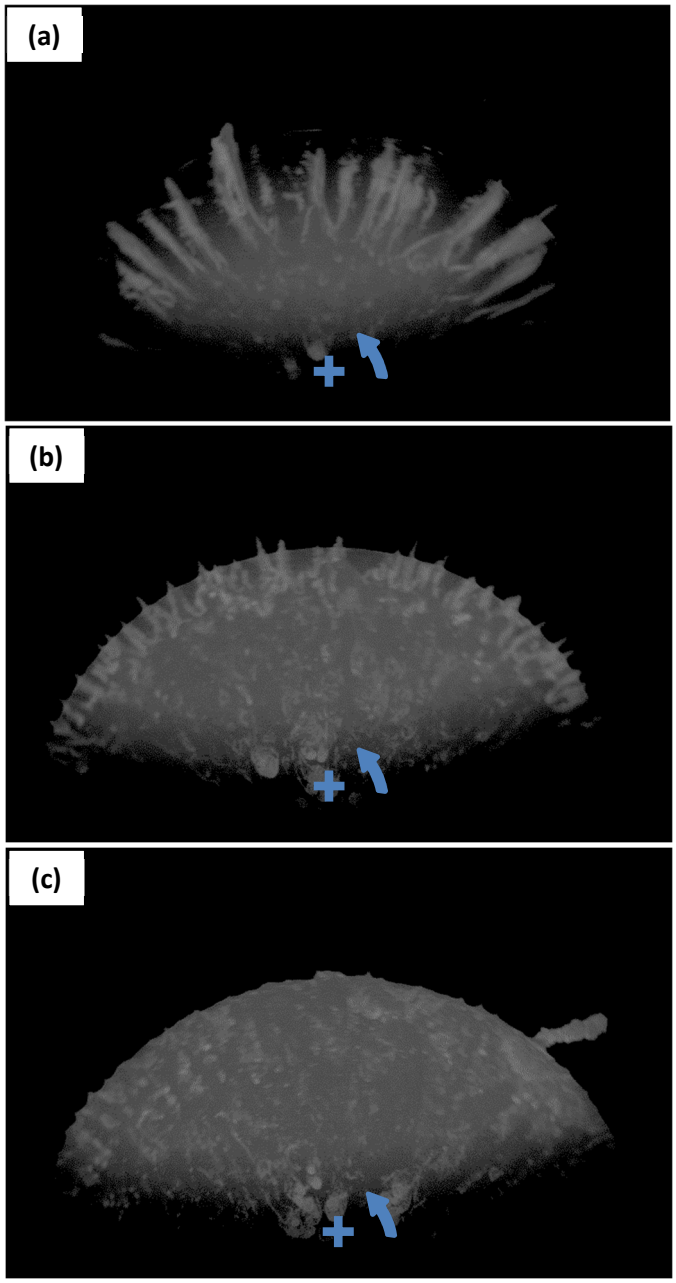

Figure 9: Infrared images of a rod atomized using an incident LASER beam power density of 8.9 W.cm^{-2} and 32.5 m.s^{-1}. Atomization times of 5.5 s, 28 s and 32 s are shown in (a), (b) and (c), respectively.

This is confirmed with temperatures that were measured at the center of the rod using a bichromatic pyrometer. Figure 10 demonstrates that a plateau is reached at the same temperature in both atmospheres, regardless of the ejection speed or the oxygen content in the surrounding atmosphere. It has to be noticed that oxygen content affects the depth of the crater in the rod, but not the temperature measurement. It can be explained by the fact that only a thin oxide film is formed and continuously remove due to the high rotational speed and the liquid flow. This mechanism induces a

higher local absorption near the edge and thus, a shallower crater in Atmosphere A without higher temperature of the metal.

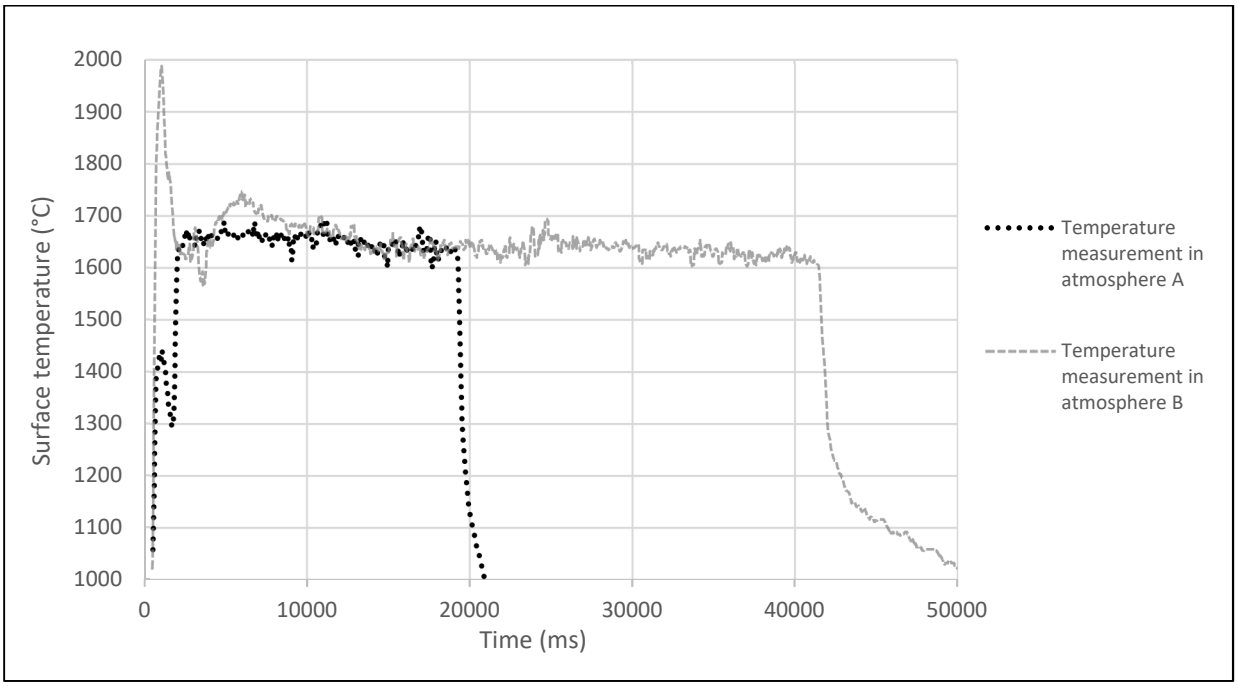

Figure 10: Temperature measurement during the atomization process using an incident LASER beam power density of 8.9 W.cm^{-2} and ejection speed of 32.5 m.s^{-1} in Atmospheres A and B.

5 Discussion

5.1 Particle size distribution

The particle size distribution of each batch was obtained by LASER diffraction analysis. Each distribution, after removing irregular particles, is monomodal and is narrow ranging between 0 to 125 µm in both atmospheres. Increasing the ejection speed reduces the mean particle size independently of the oxygen content as predicted by Equation (1) and demonstrated in studies on standard REP systems [8,13,24,25].

REP atomization of 316L grade stainless steel has been recently studied by [27]. Their atomizations were carried out at equivalent ejection speeds (31,4 m.s^{-1} – 55 m.s^{-1}) using a plasma torch. Their results are expressed in Volume Fraction and are presented in Figure 11. Our results were converted in Volume Fraction to be compared in the same table.

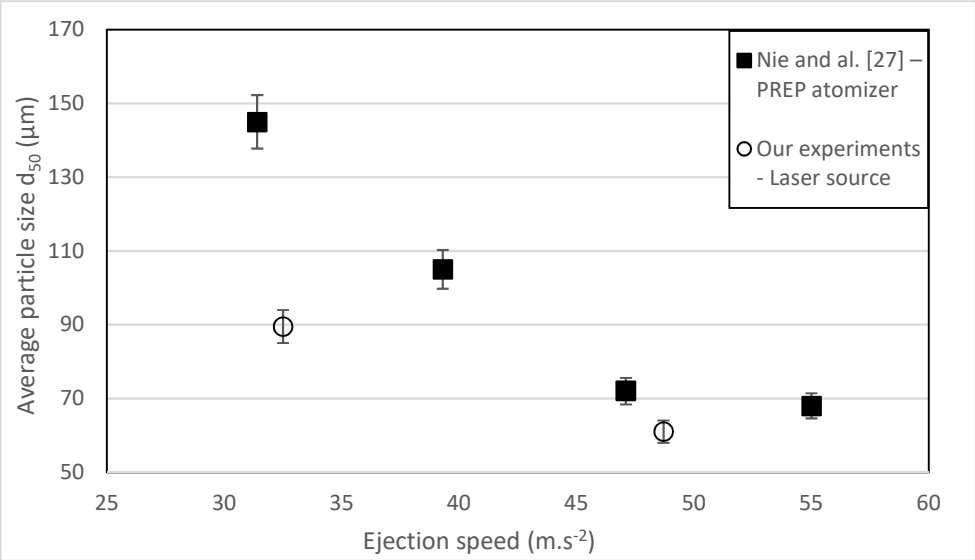

Figure 11 : Comparison of d50 measurements of 316L grade stainless steel atomized using a PREP [27] and a laser REP atomizer

D50 measurement in laser are lower than for standard PREP atomizer. At most, it can be considered that the overall values between both configurations are similar and shows good agreement.

An interesting result is that incident LASER beam power density did not affect particle size distribution, but it did have an influence on the process time and the time before the rods started to melt. K value from Equation (1) has been determined using the d_{50} value for the first atomization which used an incident LASER beam power density of 8.9 $W.cm^{-2}$ and an ejection speed of 32.5 $m.s^{-1}$ (d_{50} = 75.4 µm) in Atmosphere B. Equation (1) has been used to determine a K value of 2.53. By using this value, other calculated d_{50} values match well with experimental values obtained in Atmospheres A and B, allowing the prediction of particle size for atomization of 316L grade stainless steel powders using this atomizer configuration (Table 6). Furthermore, a part of the particle became magnetic after atomization probably due to the formation of magnetite (Fe_3O_4).

LASER Power Densities ($W.cm^{-2}$)	Ejection speed ($m.s^{-1}$)	Measured d_{50} (µm)		Calculated d_{50} (µm)
		Atmosphere A	Atmosphere B	
8.9	32.5	64.7	75.4	75.5
			75.7	
			74.9	
			75.7	
13.4		79.8	75.7	75.5
			74.6	
13.4	48.7	30.8	41.4	50.3
			36.4	

Table 6: Comparison between calculated (from Equation (1)) and measured d_{50} values by dry powder LASER granulometry of 316L grade stainless steel powders produced using different ejection speeds, incident LASER beam power densities for both Atmospheres A and B.

5.2 Irregular particles

As presented in this study, irregular particles proportions was found to be around 55 to 35 wt% depending on the parameters. For the 316L grade stainless steel, [27] found a volume fraction of irregular particles equals to 7.44 %, whereas our results are around 48,5 to 35 % in volume fractions.

For Atmosphere B, high-speed recordings show the ejection of irregular particles at the edge of the rod from a partially solidified layer. This observation is confirmed with the picture of the rod after atomization, where the edge is less melted than the center, showing a slower consumption rate of the rod at the edge. This solid layer is not visible for atomization in Atmosphere A (Figure 7). This topography can be explained by two phenomena. Firstly, the high ejection speed creates a strong convection current that cools the rod from the edge. This explanation is plausible as the external surface of the rod is larger thus enabling enhanced thermal exchanges with the surrounding atmosphere. An equivalent phenomenon was already reported for rotary disk atomization [20]. Secondly, infrared images (Figure 9) show that at the beginning of the atomization process the melting is not homogeneous. The liquid is cooled on the surface that is still not melted and produces irregular particles. Finally, the LASER energy distribution is not uniform over the whole top surface. Thus, the energy transferred at the surface replicates the Gaussian energy distribution in the LASER spot and induces the digging of a crater with less energy on the rod edge, where the liquid is cooled and produces irregular particles.

Using a 13.4 $W.cm^{-2}$ incident LASER beam power density reduces the quantity of irregular particles produced by around 15 wt %. This may be explained by the fact that a higher incident LASER beam power density achieves a sufficient level in the periphery of the LASER spot to overcome cooling induced by convection at the edge of the rod, limiting the creation of a solid layer and therefore the production of irregular particles.

This hypothesis is consistent with the results of atomization in Atmosphere A. In this condition, irregular particles only represented around 15 wt% for any incident LASER beam power density at a 32.5 $m.s^{-1}$ ejection speed. This can be explained by the oxidation of the liquid resulting in an increase of the absorptivity of the LASER energy at the periphery of the rod. Thus, it is also consistent with atomization times that are highly reduced when atomizing in Atmosphere A, since oxidation decreases the reflectivity of the surface irradiated by the LASER beam and also due to the fact that oxidation is an exothermic reaction. 20 s is necessary to atomize a 50 g rod using an 8.9 $W.cm^{-2}$ incident LASER beam power density and 32.5 $m.s^{-1}$ ejection speed in Atmosphere A, whereas 70 s is required for Atmosphere B.

5.3 Atomization regime

High-speed imaging shows that the atomization regime is affected by the oxygen content in the atmosphere. It can be observed in Figure 8 that both the DDF and LD regimes occur in Atmosphere A. This is explained by the oxidation of the molten metallic liquid which affects surface tension and/or viscosity. Oxidation of the metallic liquid tends to lower surface tension [17] and increase viscosity as a rigid oxide film is produced [23]. Both phenomena, applied in Equation (2), demonstrate that the LD regime is promoted in Atmosphere A, which is consistent with the observation. The surface condition of particles produced in Atmosphere A, presented in Figure 2, also highlights the reduction of surface tension as particles are not perfectly smooth.

In Atmosphere B, a DDF regime is achieved for each experiment. This regime is supposed to produce spherical particles within a bimodal narrow distribution. The bimodal distribution in DDF is explained by particles ejected directly from the edge of the rod that carries a small amount of liquid, which forms

smaller particles referred to as satellite particles. As shown in our results, only unimodal distribution has been measured and the formation of satellites has not been observed extensively using high-speed imaging. Satellites observed during the process are either smaller or have the same size as the main particle. Moreover, camera Sensor pixel size is 28 µm, so a smaller size particle is difficult to be observed “in-situ”. Calculations from Equation (2) predict that one experiment should take place in the LD regime, but that is not the case. As the X values are slightly over the transition value between the DDF and LD regime, this difference may be due to the lack of knowledge on liquid stainless steel properties.

6 Conclusion

A LASER source has been used successfully to replace an electrical arc in the REP process, allowing the atomization of 316L grade stainless steel powder. Particle size distributions were measured revealing a narrow unimodal distribution. These distributions shift to lower values when increasing ejection speed whereas incident LASER beam power density influences atomization time and reduces the proportion of irregular particles. Calculated d_{50} values show good agreement with measured values. High-speed recordings facilitate the understanding of the origin of irregular particles. A lack of energy at the edge of the rod induces the creation of a solid layer that disintegrates to form irregular particles during rotation.

Finally, oxygen content in the surrounding atmosphere has an important impact on the atomization regime occurring and on irregular particle production. LASER beam absorption, surface tension and viscosity properties are modified by oxidation, resulting in more dispersed measurements compared to an atmosphere with low oxygen content. The observed atomization regimes were compared with the prediction model by Hinze and Milborn [18]. A good agreement is found between observed and predicted values taking into account that some liquid 316L grade stainless steel properties may not be well known leading to little shift in the prediction calculation.

Abstract

316L grade stainless steel powders were produced by centrifugal atomization during the melting of a rotating rod heated by a high-power LASER beam. The feasibility has been demonstrated by atomizing a range of stainless steel rods. The atomization process has been observed via high-speed imaging and fragmentation regimes have been identified according to a literature review on the rotating electrode process (REP). Results were compared with literature data and an existing prediction model for such a process. High-speed observation can monitor the present process and it is shown that a solidified layer of metal is formed at the edge of the rod during the process inducing metal flake ejection due to the centrifugal stresses. Effects of incident LASER beam power density, ejection speed and oxygen content of the surrounding atmosphere on the particle size distribution and the sample surface have been studied and compared with literature data on classical REP atomizers. The study focuses on the production of irregular particles during the atomization process and highlights the influence of the oxygen content in the surrounding atmosphere on the fragmentation regime and the resulting particle size distribution.

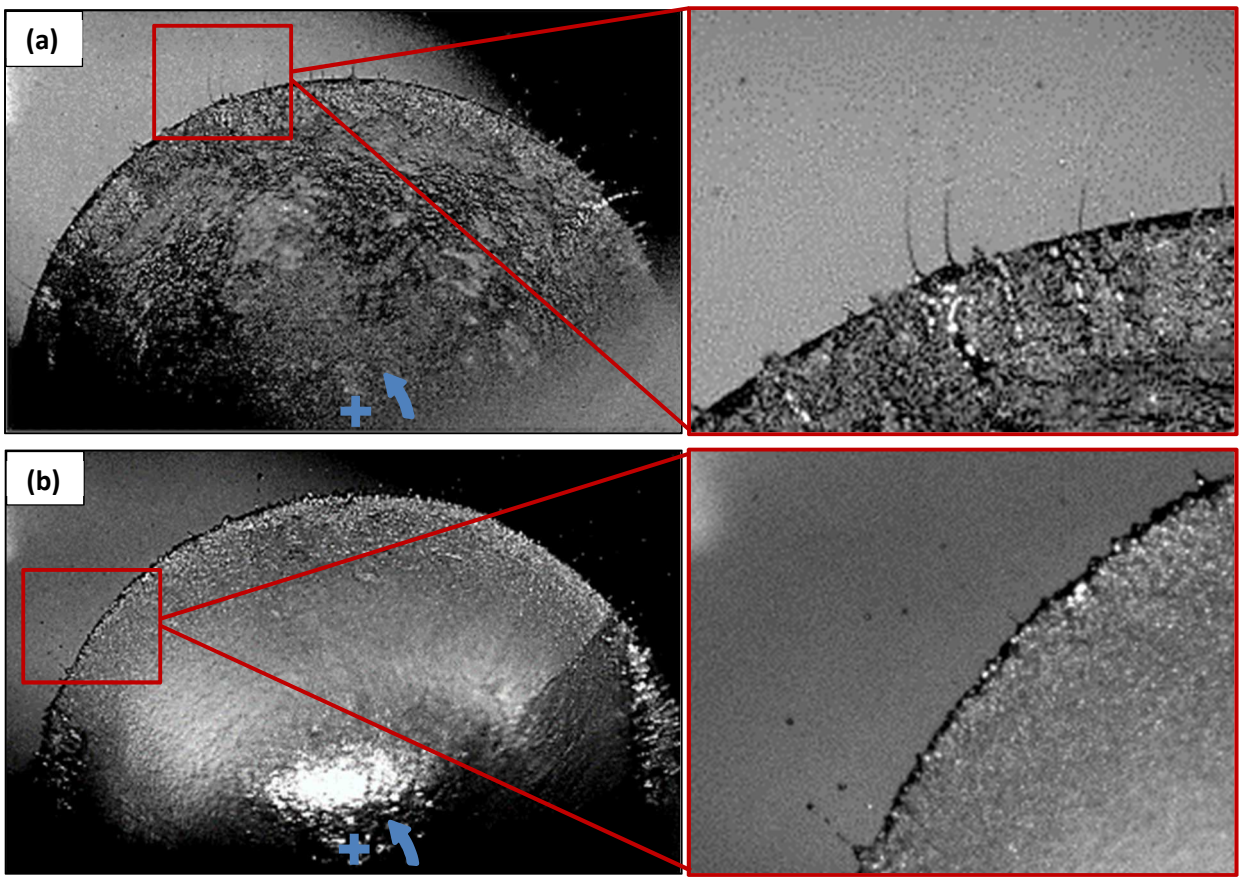

High-speed images were recorded during the atomization of 316L grade stainless steel rods. (a) shows a hybrid DDF/LD regime in Atmosphere A for an 8.9 W.cm^{-2} incident LASER beam power density and 32.5 m.s^{-1} ejection speed. (b) displays a DDF regime in Atmosphere B for a 13.4 W.cm^{-2} incident LASER beam power density and 48.7 m.s^{-1} ejection speed.

Keywords: LASER, Atomization, Particle Size, REP, High-speed imaging

Acknowledgements:

The authors would like to thank the Association Nationale de la Recherche et de la Technologie (ANRT) and the Région Bourgogne Franche-comté for their financial support.

7 References

[1] Y. Millet, Fabrication de poudres métalliques par la méthode PREP®, Techniques de l'ingénieur Procédés de fabrication additive. Internal base : TIB633DUO (2015). https://www.techniques-ingenieur.fr/base-documentaire/mecanique-th7/procedes-de-fabrication-additive-42633210/fabrication-de-poudres-metalliques-par-la-methode-prep-in221/.

[2] R. Meyer, Poudres métalliques, Techniques de l'ingénieur Mise en forme des métaux et fonderie. (1980). https://www.techniques-ingenieur.fr/base-documentaire/archives-th12/archives-mise-en-forme-des-metaux-et-fonderie-tiamc/archive-1/poudres-metalliques-m862/.

[3] R.-P. Guo, L. Xu, B.Y.-P. Zong, R. Yang, Characterization of Prealloyed Ti–6Al–4V Powders from EIGA and PREP Process and Mechanical Properties of HIPed Powder Compacts, Acta Metallurgica Sinica (English Letters). 30 (2017) 735–744. https://doi.org/10.1007/s40195-017-0540-4.

[4] G. Chen, S. Zhao, P. Tan, J. Yin, Q. Zhou, Y. Ge, Z. Li, J. Wang, H. Tang, P. Cao, Shape memory TiNi powders produced by plasma rotating electrode process for additive manufacturing, Transactions of Nonferrous Metals Society of China. 27 (2017) 2647–2655. https://doi.org/10.1016/S1003-6326(17)60293-0.

[5] O.D. Neikov, ed., Handbook of non-ferrous metal powders: technologies and applications, 1. ed, Elsevier, Amsterdam, 2009.

[6] G. Chen, S.Y. Zhao, P. Tan, J. Wang, C.S. Xiang, H.P. Tang, A comparative study of Ti-6Al-4V powders for additive manufacturing by gas atomization, plasma rotating electrode process and plasma atomization, Powder Technology. 333 (2018) 38–46. https://doi.org/10.1016/j.powtec.2018.04.013.

[7] Y. Chen, J. Zhang, B. Wang, C. Yao, Comparative study of IN600 superalloy produced by two powder metallurgy technologies: Argon Atomizing and Plasma Rotating Electrode Process, Vacuum. 156 (2018) 302–309. https://doi.org/10.1016/j.vacuum.2018.07.050.

[8] F. Průša, D. Vojtěch, A. Michalcová, I. Marek, Mechanical properties and thermal stability of Al–Fe–Ni alloys prepared by centrifugal atomisation and hot extrusion, Materials Science and Engineering: A. 603 (2014) 141–149. https://doi.org/10.1016/j.msea.2014.02.081.

[9] J.O. Yin, G. Chen, S.Y. Zhao, Y. Ge, Z.F. Li, P.J. Yang, W.Z. Han, J. Wang, H.P. Tang, P. Cao, Microstructural characterization and properties of Ti-28Ta at.% powders produced by plasma rotating electrode process, Journal of Alloys and Compounds. 713 (2017) 222–228. https://doi.org/10.1016/j.jallcom.2017.04.195.

[10] S. Öztürk, F. Arslan, Production of rapidly solidified metal powders by water cooled rotating disc atomisation, Powder Metallurgy. 44 (2001) 171–176. https://doi.org/10.1179/003258901666220.

[11] D.G. Konitzer, K.W. Walters, E.L. Heiser, H.L. Fraser, Rapidly solidified prealloyed powders by laser spin atomization, Metallurgical Transactions B. 15 (1984) 149–153. https://doi.org/10.1007/BF02661073.

[12] T.C. Peng, S.M.L. Sastry, J.E. O'neal, Laser-melting/spin-atomization method for the production of titanium alloy powders, Metallurgical Transactions A. 16 (1985) 1897–1900. https://doi.org/10.1007/BF02670377.

[13] B. Champagne, R. Angers, Fabrication of powders of powders by the rotating electrode process, International Journal of Powder Metallurgy and Powder Technology. 16 (1980) 359–367.

[14] A. Lawley, Atomization: the production of metal powders, Metal Powder Industries Fed., Princeton, NJ, 2003.

[15] M. Zdujić, D. Uskoković, Production of atomized metal and alloy powders by the rotating electrode process, Soviet Powder Metallurgy and Metal Ceramics. 29 (1990) 673–683. https://doi.org/10.1007/BF00795571.

[16] L. Tian, I. Anderson, T. Riedemann, A. Russell, Production of fine calcium powders by centrifugal atomization with rotating quench bath, Powder Technology. 308 (2017) 84–93. https://doi.org/10.1016/j.powtec.2016.12.011.
[17] N. Eustathopoulos, B. Drevet, Tension superficielle des métaux liquides et capillarité, Techniques de l'ingénieur Données physico-chimiques sur les métaux et alliages. Internal base : TIB530DUO (2017). https://www.techniques-ingenieur.fr/base-documentaire/materiaux-th11/donnees-physico-chimiques-sur-les-metaux-et-alliages-42530210/tension-superficielle-des-metaux-liquides-et-capillarite-m67/.
[18] J.O. Hinze, H. Milborn, Atomization of Liquids by Means of a Rotating Cup, Journal of Applied Mechanics. (1950) 9.
[19] B. Champagne, R. Angers, REP Atomization Mechanisms, Powder Metallurgy International. 16 (1984) 125–128.
[20] R. Angers, R. Tremblay, D. Dubé, Formation of irregular particles during centrifugal atomization of AZ91 alloy, Materials Letters. 33 (1997) 13–18. https://doi.org/10.1016/S0167-577X(97)00072-4.
[21] J. Tang, Y. Nie, Q. Lei, Y. Li, Characteristics and atomization behavior of Ti-6Al-4V powder produced by plasma rotating electrode process, Advanced Powder Technology. 30 (2019) 2330–2337. https://doi.org/10.1016/j.apt.2019.07.015.
[22] Thyssenkrupp Materials (UK), Stainless Steel 316L - 1.4404 Data Sheet -, Thyssenkrupp Materials (UK). (n.d.). https://www.thyssenkrupp-materials.co.uk/stainless-steel-316l-14404.html (accessed January 13, 2021).
[23] L. Lucas, Viscosité des principaux métaux et métalloïdes, Techniques de l'ingénieur Bases de données : matériaux métalliques. Internal base : TIB584210 (1984). https://www.techniques-ingenieur.fr/base-documentaire/materiaux-th11/bases-de-donnees-materiaux-metalliques-42584210/viscosite-des-principaux-metaux-et-metalloides-m66/.
[24] R. Yamanoglu, R.M. German, S. Karagoz, W.L. Bradbury, M. Zeren, W. Li, E.A. Olevsky, Microstructural investigation of as cast and PREP atomised Ti–6Al–4V alloy, Powder Metallurgy. 54 (2011) 604–607. https://doi.org/10.1179/1743290110Y.0000000006.
[25] H. Li, X. Deng, Prediction of powder particle size during centrifugal atomisation using a rotating disk, Science and Technology of Advanced Materials. 8 (2007) 264–270. https://doi.org/10.1016/j.stam.2007.03.001.
[26] R. Indhu, V. Vivek, L. Sarathkumar, A. Bharatish, S. Soundarapandian, Overview of Laser Absorptivity Measurement Techniques for Material Processing, Lasers Manuf. Mater. Process. 5 (2018) 458–481. https://doi.org/10.1007/s40516-018-0075-1.
[27] Y. Nie, J. Tang, B. Yang, Q. Lei, S. Yu, Y. Li, Comparison in characteristic and atomization behavior of metallic powders produced by plasma rotating electrode process, Advanced Powder Technology. 31 (2020) 2152–2160. https://doi.org/10.1016/j.apt.2020.03.006.

Centrifugal atomization of stainless-steel by high power LASER beam and high-speed imaging

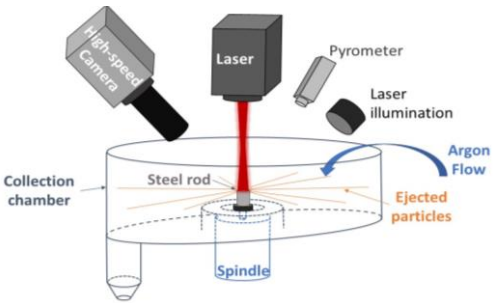

→ More homogeneity in melting rods

→ Less pollution from heat source

→ Allows monitoring of the process up to 30,000 frames per second

Powders characteristics

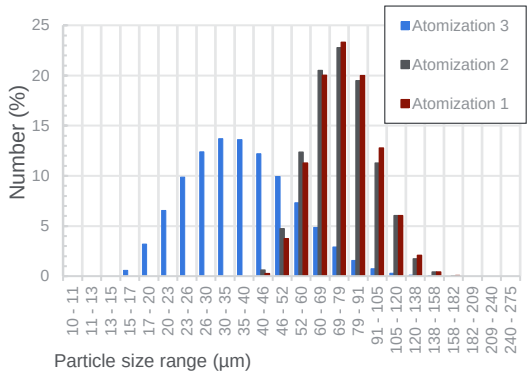

Particle size distribution of 316L at different rotational speeds and Laser powers

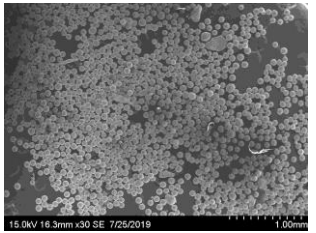

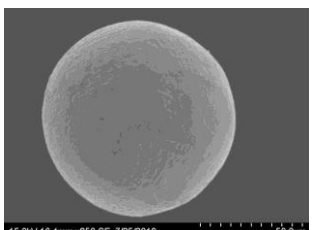

SEM Observations

High-speed imaging

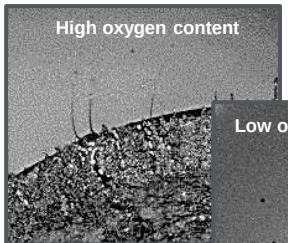

Atomization regimes

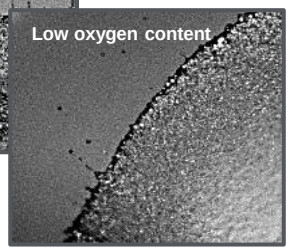

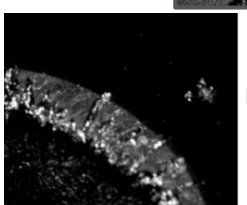

Irregular particle production

Ravry and al., 2022

Conclusions:

→ **Feasibility of using a LASER as heat source and observe atomization regime in centrifugal atomization**
→ **Unimodal Particle Size Distributions (PSD) and highly spherical particles**
→ **Production of irregular particles from a solid layer**
→ **Oxygen content affect atomization regime and irregular particle production**